Journal of Structural Geology 31 (2009) 315–327

Contents lists available at ScienceDirect

Journal of Structural Geology

journal homepage: www.elsevier.com/locate/jsg

Numerical modelling of strain localisation and fluid flow during extensional fault reactivation: Implications for hydrocarbon preservation

Y. Zhang [a,*], A. Gartrell [b,1], J.R. Underschultz [b], D.N. Dewhurst [b]

[a] CSIRO Exploration & Mining, PO Box 1130, Bentley, WA 6102, Australia
[b] CSIRO Petroleum Resources, PO Box 1130, Bentley, WA 6102, Australia

ARTICLE INFO

Article history:
Received 31 July 2008
Received in revised form
24 October 2008
Accepted 7 November 2008
Available online 27 November 2008

Keywords:
Fault reactivation
Extension
Fluid flow
Hydrocarbon preservation
Timor Sea

ABSTRACT

A numerical modelling approach is used to investigate the main controls of strain localisation on faults and fluid flow in fault-bound reservoir rocks during extensional reactivation. A series of 3D coupled mechanical deformation and fluid flow models were performed to simulate the response of simple fault and reservoir-seal geometries to extensional reactivation. The model results demonstrate that initial fault length is a primary control on strain distribution between faults and on fluid transport from the reservoir through the top seal. During extensional reactivation, longer faults in the population tended to accommodate greater shear strain and accumulate greater throw than smaller faults. With greater length contrast, there is an increased throw contrast for the same amount of extension. This behaviour can be attributed to the mechanism of strain sharing among fault elements. Spacing between adjacent faults is a secondary factor affecting strain partitioning. For a given fault length contrast, increasing the spacing increases the freedom of adjacent faults to move and leads to a more even distribution of strain. Fault strike overlap styles also affect strain distribution along faults. This is mainly expressed as the reduction of throws in the overlapping fault segments and partially overlapped or adjacent fault ends. Our models further demonstrate that fault lengths are likely to control fluid flow during extensional reactivation. Large faults in the models are the main conduit for fluid transport, expressed as strong upward fluid flow along these faults from the sandstone reservoir horizon through the shale seal.

1. Introduction

Fault reactivation and associated seal breach can severely reduce the integrity of hydrocarbon traps, and therefore, represents a major risk for hydrocarbon exploration in some settings. In the Timor Sea, the primary hydrocarbon traps are developed in extensional fault blocks, initially formed during Jurassic rifting, sealed by Late Jurassic and Early Cretaceous shales. Structural analyses from the Timor Sea indicate that the majority of these rift-phase were reactivated during the Late Tertiary extensional event, resulting in widespread top seal breach and hydrocarbon leakage (e.g. O'Brien et al., 1999; Gartrell et al., 2006). However, the distribution of strain within the regional fault population is heterogeneous. This strain heterogeneity appears to be the critical control determining whether a given fault-bound trap preserves a significant hydrocarbon column or not (e.g. Gartrell et al., 2005, 2006). To advance our understanding of the major controls on fault deformation and their impact on fluid flow in reservoirs during extensional reactivation from fault attributes, we have constructed a series of coupled mechanical deformation and fluid flow numerical models containing simple fault geometries. We aim to achieve a systematic assessment of how key factors, such as fault length, spacing and alignment styles, influence strain distribution patterns and fluid flow along faults during extensional reactivation. Knowledge of these behaviours will aid trap integrity prediction where extensional fault reactivation has occurred.

Fault reactivation and fluid flow associated with faults have attracted extensive study in the fields of economic geology and petroleum geology. Sibson (1985) pointed out that most of intra-plate deformation in the frictional seismogenic regime is accommodated by the reactivation of existing faults and proposed conceptual stress conditions for fault reactivation. One stream of published studies is concerned with the reactivation behaviours of faults under strike-slip and compressional regimes. For example, Cox (1995) described the reverse-faulting reactivation of a natural fault under low shear stress and high fluid pressure conditions and

* Corresponding author. Tel.: +61 8 6436 8626; fax: +61 8 6436 8555.
E-mail address: yanhua.zhang@csiro.au (Y. Zhang).
[1] Present address: Brunei Shell Petroleum, BSP Head Office, Seria, KB 3534, Brunei.

0191-8141/$ – see front matter Crown Copyright © 2008 Published by Elsevier Ltd. All rights reserved.
doi:10.1016/j.jsg.2008.11.006

suggested a process of multiple episodes of fluid flow along the fault. Connolly and Cosgrove (1999a, 1999b) investigated stress patterns around dilatant fault jogs under strike-slip conditions and inferred fluid flow patterns based on mean stress patterns from photoelastic analogue experiments. The analogue models of McClay and Bonora (2001) illustrated the formation of "flower" structures at fault stepovers as a result of reactivation of strike-slip fault systems. Using a numerical modelling approach, Zhang et al. (2008) simulated rock dilation and fluid flow localisation around fault dilation jogs under compressional and strike-slip reactivation conditions.

Walsh et al. (2001) examined the growth of normal fault arrays and showed that fault displacement rates correlate with fault size with displacement localised onto larger faults, based on interpretation of seismic sections (e.g. the Timor Sea) and their particle-material normal fault models. Walsh et al. (2002) further presented an alternative model for the growth of normal faults, suggesting near-constant fault lengths with the growth essentially accommodated by displacement (i.e. increase in displacement/length ratio). Stewart (2001) described a positively correlated relationship between the fault-parallel stretches of beds and the displacement/length ratio. In consideration of interaction between extensional deformation and fluid flow in faults, McLellan et al. (2004) numerically simulated deformation and fluid flow in an extensional basin model containing one shallow dipping fault, a structural scenario for the Hamersley Basin. Gartrell et al. (2004) also numerically modelled extensional reactivation of a triple fault intersection, a typical structure in the Timor Sea, and further discussed potential hydrocarbon leakage for such fault architecture. In an effort to simulate complex natural basin and fault systems, Buchmann and Connolly (2007) and Buchmann et al. (2008) modelled the complex 3D structures of the Upper Rhine Graben and predicted stress and fault reactivation under transtensional conditions.

Another stream of numerical modelling work focuses on geothermal and buoyancy driven fluid convection along faults in sedimentary basins without consideration of effects of deformation (e.g. Garven et al., 2001; Yang et al., 1998, 2004). The results of these models describe fluid circulation along permeable faults in sedimentary basins before reactivation.

Although extensive work on fault reactivation and fluid flow along faults has been carried as summarized above, several key factors (i.e. fault length, spacing and strike-overlap or alignment styles) that could affect strain partitioning and fault movement in a fault population under extensional settings still needs further systematic work. This is particularly important for the evaluation of trap integrity and hydrocarbon preservation, which is the focus of the present study.

2. Modelling methodology

The 3D finite difference code, FLAC3D (Fast Lagrangian Analysis of Continua) was used in this study (Cundall and Board, 1988; Itasca, 2005). This code is capable of simulating the interactions between deformation and fluid flow in porous media. Rock materials are represented by a 3D mesh consisting of hexahedral elements. A mesh can be generated with numerous regions to fit the geometries of the geological structures to be simulated. Each element in the mesh behaves according to prescribed mechanical and hydraulic laws in response to the applied boundary conditions. The material can yield and deform plastically and the mesh deforms and moves with the material. The explicit Lagrangian computation scheme adopted by FLAC3D, together with the mixed-discretization technique and dynamic relaxation scheme, ensure that plastic failure, flow and deformation localisation are modelled accurately (Cundall and Board, 1988; Itasca, 2005). The code has been applied to, for example, the fields of structural geology (e.g. Hobbs et al., 1990; Ord, 1991; Zhang et al., 2000; Strayer et al., 2001) and economic geology (Sorjonen-Ward et al., 2002; McLellan et al., 2004; Schaubs et al., 2006; Zhang et al., 2006).

Detailed description of the constitutive laws and mathematics adopted in FLAC3D can be found in Itasca (2005), Cundall and Board (1988), Strayer et al. (2001), McLellan et al. (2004) and Ord (1991). The rocks in the current FLAC3D models are simulated as Mohr–Coulomb isotropic elastic–plastic materials (Itasca, 2005; Cundall and Board, 1988; also see Vermeer and de Borst, 1984; Strayer et al., 2001). The involved constitutive parameters include shear modulus (G), bulk modulus (K), cohesion (C), tensile strength (T), friction angle (φ) and dilation angle (ψ). Under loading, such materials deform initially in an elastic manner up to a yield point defined by the Mohr–Coulomb yield criteria (i.e. before the maximum shear stress reaches a threshold magnitude), after which it deforms in a plastic manner. In addition, tensile failure occurs when the effective minimum principal stress is in tension and overcome tensile strength. Dilatancy (positive volume change) is an important feature of the present model, which occurs with shear deformation of a material. The dilatant potential of the Mohr–Coulomb material for plastic deformation is characterized by the dilation angle (ψ). FLAC3D adopts the engineering stress-sign convention, that is, compressive stress is assumed negative and tensile stress is positive.

Fluid flow in the models is governed by Darcy's law (Itasca, 2005; also see Mandl, 1988; Strayer et al., 2001; McLellan et al., 2004) for an isotropic porous medium. As such, fluid flow velocities are primarily a function of gradients in pore fluid pressures and variations in permeability. Fluid flow is coupled with mechanical deformation during a simulation.

The interactions between mechanical deformation and fluid flow are mainly reflected through four aspects during modelling. First, volumetric strain or solid volume changes result in pore pressure changes. For example, a local volume increase or dilation leads to a local pore pressure decrease. The variations of fluid pore pressure changes as a function of solid volume changes or volumetric strains represent the most important aspect of deformation–fluid flow coupling. Second, changes in pore pressure cause changes in effective stress, which further affect the response of the solid (e.g. a reduction in effective stress may induce plastic yield). Third, the formation of any topographic elevation or depression in a model, as a result of bulk deformation, can change pore pressure or head distribution, and then lead to changes in fluid flow patterns. Finally, mechanical deformation could lead to permeability enhancement and hence change fluid flow patterns. In this study, we have adopted a simple approach to allow fault permeability to change with shear strain (see below for details). It needs to be mentioned that the current models do not simulate the explicit changes of rock porosities (Table 1). However, the actual total pore volume of a model during deformation is defined by initial porosities and volume changes or volumetric strains. See Itasca (2005) and McLellan et al. (2004) for more detailed description of deformation and fluid flow coupling in FLAC3D.

3. Model description

3.1. Model architecture: stratigraphy and faults

The present models have been constructed for a regional scale with a model size of 50 by 50 km in plan-view and 10 km in depth. This model size is appropriate to investigate regional structural control on fault reactivation in the Timor Sea (Gartrell et al., 2006). The models consider a simple fault system consisting of two faults

Table 1
Initial material properties of the models.

Model unit	Density ($kg\ m^{-3}$)	Young's modulus (Pa)	Poisson's ratio	Cohesion (Pa)	Tensile strength (Pa)	Permeability (m^2)	Porosity	Friction angle (°)
Carbonate	2500	4.0×10^{10}	0.2	1.75×10^{7}	8.75×10^{6}	5.0×10^{-15}	0.3	30
Shale	2400	2×10^{9}	0.35	2.75×10^{6}	1.375×10^{6}	1.0×10^{-19}	0.15	22
Sandstone	2450	2.5×10^{10}	0.25	1.5×10^{7}	7.5×10^{6}	1.0×10^{-14}	0.18	30
Basal unit	2550	2.0×10^{9}	0.2	2.0×10^{6}	1.0×10^{6}	1.0×10^{-19}	0.05	20
Faults	2300	1.0×10^{9}	0.15	1.0×10^{6}	0.5×10^{6}	Various	0.2	15

(Fig. 1), one larger and one smaller; for example, one fault strike length combination is 30 and 6 km. The two fault planes are either parallel (Fig. 1a), or cross-cutting (Fig. 1b). Various sub-sets of models have been constructed to explore the effects of variations in fault length, fault spacing and fault strike overlap geometries. All the faults modelled here dip initially at 65° and are represented by relatively narrow fault zones (~270 m thick).

The stratigraphy of these models is also quite simple, consisting of four rock units (Fig. 1). They are, from top to bottom: 1) a carbonate layer; 2) a relatively thin shale layer; 3) a sandstone unit (reservoir rock); and 4) a relatively soft basal rock unit as a more ductile domain. The incorporation of rock unit 4 is aimed to avoid a situation where faults reach the model base and thus reduce the edge effects of the model bottom boundary on fault movement. It should be pointed out that such a stratigraphic sequence represents a simplification of regional stratigraphy in the Timor Sea, which has rather variable thickness. In particular, thickness variation for the sandstone unit (a generally thicker and deeper rock unit) can be quite large in the region. In our models presented here, the bottom boundary of the sandstone unit sits at a depth level of 5 km. Details of rock unit thicknesses are given in Fig. 1 (see figure caption).

Our models also simulate a simple structural relationship between faults and stratigraphy. The lower tips of all the faults reach the bottom boundary of the sandstone unit, but the top tips are located at two different depth levels (Fig. 1). The larger fault reaches the top of the model (the surface), in contrast, the smaller fault is buried within the carbonate unit ("blind" fault). These

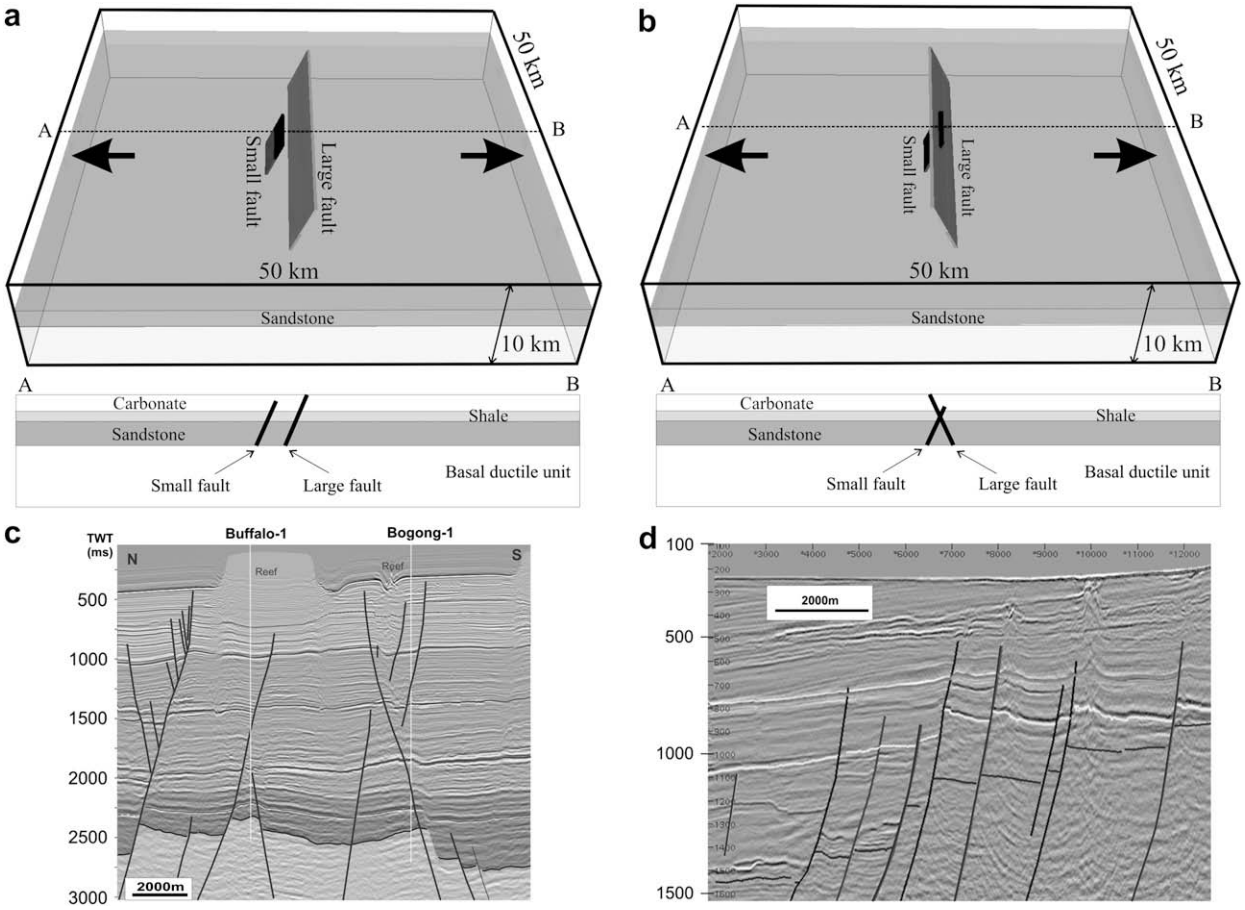

Fig. 1. 3D and section views of initial geometries of two models. (a) A model with two parallel faults (spacing between the two faults is 2.5 km). (b) A model with two cross-cutting faults. The lengths of the large and small faults are 30 and 6 km, respectively. Arrows indicate extension direction (normal to faults). The 3D diagrams only show one rock unit (sandstone) for better visibility of faults. The section plots are along the A–B line. The thicknesses of stratigraphic units are: ~2050 m (carbonate), ~900 m (shale), ~2050 m (sandstone) and 5000 m (basal unit). (c) and (d) Illustrate examples of fault geometries from the Timor Sea and the North West Shelf (seismic sections and interpretation); high angle dipping lines illustrate fault traces in cross-sections.

structural relationships are commonly observed in the Timor Sea and the Northwest Shelf (e.g. Gartrell et al., 2006; see Fig. 1c and d).

3.2. Mechanical and hydrological properties

Rock mechanical and fluid flow properties are listed in Table 1. These parameters are selected, based on rock property data for the region (unpublished data from the Integrated Predictive Evaluation of Traps and Seals Consortium – IPETS) or from literature. Note that the bulk and shear moduli of the rocks (not included in Table 1) are related to the Young's modulus and Poisson's ratio according to the linear equations commonly defined for elastic or elastic–plastic materials (e.g. equations on page 111 of Jaeger and Cook, 1979).

In the models, faults are simulated as narrow weak zones with decreased strength parameters (see Table 1). We have also incorporated a fault permeability variation scheme in the models, by which fault permeabilities increase with accumulation of shear strain during extensional reactivation. More specifically, the permeabilities of faults are initially identical to those of host rocks (Table 1). The maximum increase of fault permeability with shear strain is determined by the following rule in respective host rocks: 1) 2.0×10^{-14} m^2 in carbonate; 2) 1.0×10^{-15} m^2 in shale; 3) no change in sandstone and soft basal unit (i.e. still 1.0×10^{-14} and 1.0×10^{-19} m^2, respectively). This is a very simple permeability enhancement scheme as an attempt to capture the behaviour of permeability increase with initial shear accumulation along faults; fluid flow will be sensitive to such permeability-shear strain relationship. It is consistent with the general expectation that low permeability rocks should experience porosity/permeability increase when involved in shearing deformation (e.g. shearing fractured shale) and also consistent with the experimental results of Zhang and Cox (2000) showing permeability enhancement in a synthetic mud with shearing deformation. Note that this scheme does not allow any permeability reduction, which might happen at higher shear strain states in faults (e.g. Holland et al., 2006). But this approximation is reasonable for the present models because the models only consider relatively small bulk extension (see below).

3.3. Boundary conditions

Initial fluid pore pressures represent an important boundary condition for fluid flow in the models. We have adopted one condition of initial head and pore pressure gradients based on data from the Timor Sea. This condition represents a slightly over-pressured system in the rocks below the carbonate layer (Fig. 2). In more details, a hydrostatic fluid pressure gradient is specified for the carbonate layer at the top of the models. Pore pressures for deeper sequences are approximately 8% (in shale) and 1.5% (in sandstone and basal unit) greater than the hydrostatic gradient. In addition, the initial pore pressure gradient is fixed at the left and right hand (see Fig. 1) boundaries of the model down to the base of sandstone layer, approximately simulating the regional hydraulic gradient of the basin driven by compaction (Otto et al., 2001; Underschultz et al., 2002).

All the models are subject to extensional deformation with a constant extensional displacement rate of 1.0×10^{-8} m/s

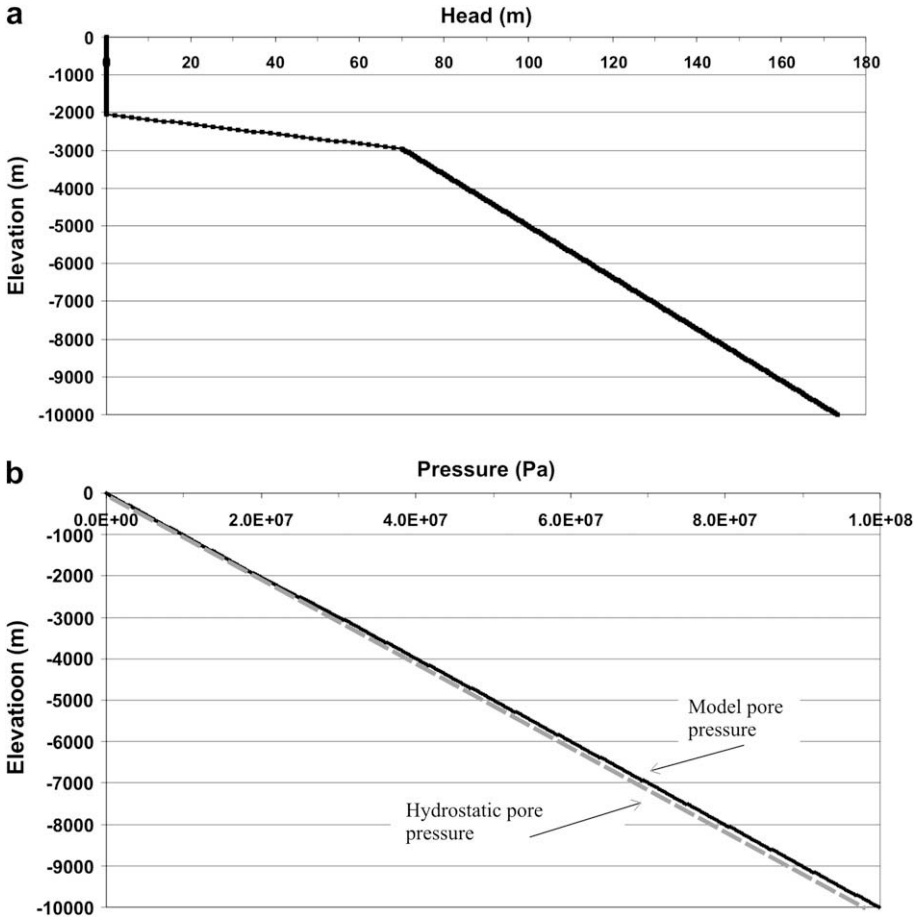

Fig. 2. Hydraulic head (a) and pore pressure (b) gradients for the present models. These gradients represent a slightly over-pressured system in the rocks below the carbonate unit.

(time here refers to fluid flow time) applied normal to the left and right edges of the models (Fig. 1). This approximately corresponds to an extensional strain rate of 4×10^{-13}. The other key mechanical boundary conditions include: 1) the top of the model is simulated as a free surface; 2) the front and back edges of the models are not allowed to move in the direction normal to the direction of extension; and 3) the base of the model is not allowed to move in the vertical direction. Free movement is allowed in other directions not specified above. All the models are deformed to a maximum 3% bulk extension; the regional bulk extension for the Late Tertiary extensional reactivation in the Timor Sea is most likely less than 2%.

4. Model results

4.1. Fault length controls on strain distribution

The current model results show that the initial lengths of faults are the primary control in determining strain partitioning between the members of a fault population. The basic features of strain distribution can be illustrated by a pair of the correlating models with two parallel faults and two cross-cutting faults, respectively (Fig. 1). The two faults in each of the two cases (i.e. parallel and cross-cutting faults) have large length contrast, with the larger fault being 30 km long and the smaller fault being 6 km. Deformed geometries, shear strain, volumetric strain and displacement vectors at 1.5% bulk extension are presented in Fig. 3. The results of both models consistently show that the large fault accommodated much of the bulk extension. This is reflected by large normal fault offset and subsidence (see deformed geometries and patterns of displacement vectors in Fig. 3) of the hanging-wall rocks along the large fault and the accumulation of much higher shear strain within the larger fault. In contrast, the smaller fault is shown to have generated little offset and accumulated very minor shear strain. In the model with two cross-cutting faults (Fig. 3b), the smaller fault is clearly displaced by the large fault. The larger fault also accumulated greater volumetric strain in both the parallel and cross-cutting fault cases than the smaller fault (i.e. within fault zone). The largest positive volumetric strain (dilation) generally occurred near the top tips of the faults, a location where the some drop of the hanging-wall block occurred in contrast to the relative elevation of the footwall block. It is noted that in the parallel-fault model (Fig. 3a), very high dilation occurred in host rocks immediately above the top tip of the smaller fault, reflecting mechanical perturbation of faulting slip in adjacent host rocks, but this did not occur above the top tip of the larger fault due to its exposure at the surface. Note that because the extension direction of the models is perpendicular to fault strike, there is no strike-slip movement along the faults in the models and the strain patterns entirely reflect the effects of normal faulting displacement.

Examination of shear strain development in fault zones versus model bulk extensional strain (Fig. 4) suggests there was a change in strain rate during extensional fault reactivation. In the pre-failure stage, the rates of strain accumulation in large and small faults are similar. But, subsequent development is characterized by: 1) the large fault failing earlier than the small fault; 2) both faults experiencing strain rate increase immediately post-failure; and 3) strain rate for the large fault displaying further increase approximately after 1% bulk extension, whereas the small fault shows some strain rate decrease for the corresponding stage. Such characteristics of strain rate evolution are consistent with greater strain accumulation in the large fault.

Analyses of fault throw (the vertical component of fault displacement) along the initial length of a fault provide useful information about the relationship between fault length and fault movement. Fig. 5a plots the distributions of fault throw along fault length (plotted as distance) at 1.5% bulk extension for the model containing two parallel faults with strike lengths of 6 and 30 km, respectively (Fig. 1a). There is a large contrast in fault throw between the large and small faults. The large fault attains a maximum throw of about 147 m and a minimum throw of 72 m,

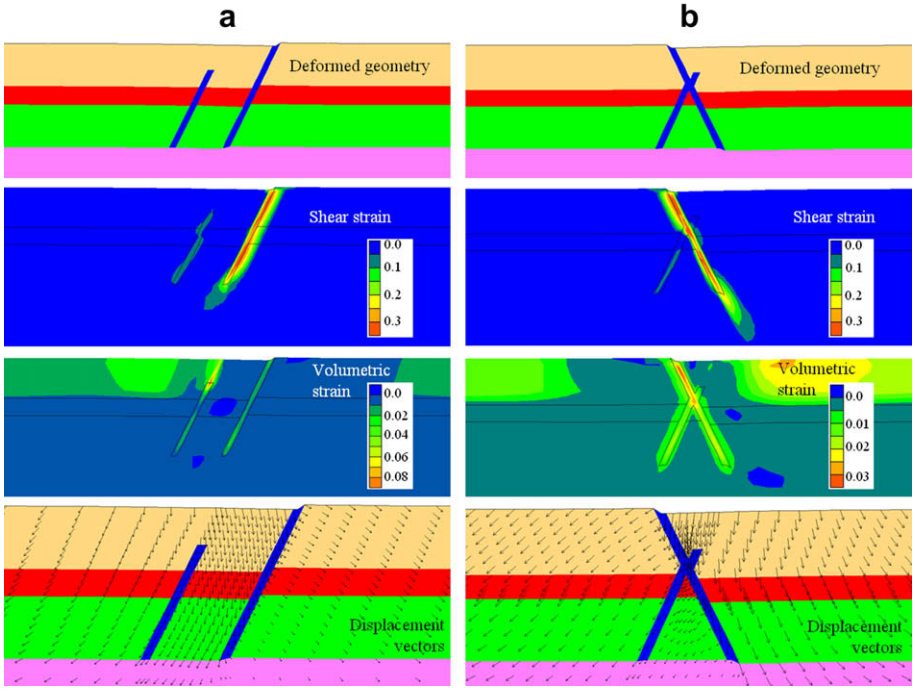

Fig. 3. Deformation patterns (deformed geometries, shear strains, volumetric strains and displacement vectors) for two models. (a) A model with two parallel faults (spacing = 2.5 km). (b) A model with two cross-cutting faults. The small and large faults in both models are 6 and 30 km long. Plotted section is through the middle of the models (see the A–B line in Fig. 1). The larger faults show greater shear displacement and offset than the smaller faults.

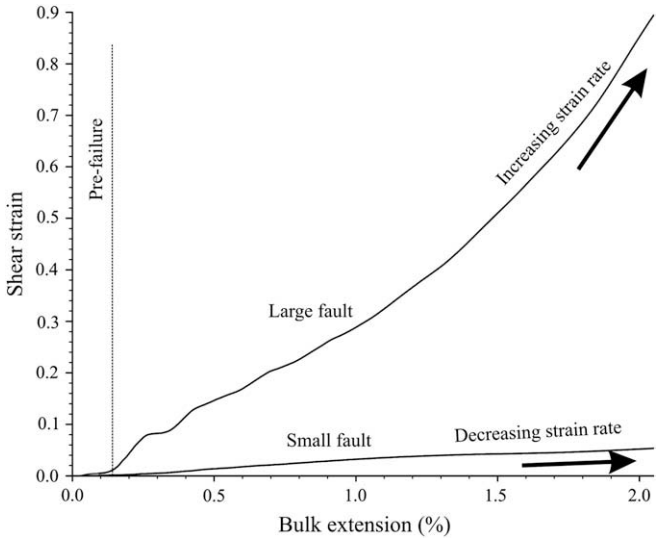

Fig. 4. Variations of shear strain in faults versus bulk extensional strain for a model with two parallel faults (see Fig. 1a for model initial geometries and Fig. 3a for model strain deformation patterns). Fault lengths are 6 and 30 km with a spacing of 2.5 km. Data tracking locations are within faults at the shale horizon.

whereas the small fault attains a maximum throw of 32 m and a minimum throw of only 1.7 m. Both faults have a smooth arched throw profile, with the maximum at the central location of the faults and diminishing throw values towards the initial fault tips. It needs to be mentioned that fault throws have only been recorded over the original length of the faults. Although the current continuum models do not explicitly simulate the propagation of faults, some shear strain localisation and displacement does occur at the tips of faults. The minimum throws shown here are located at fault tips and reflect the effect of potential fault propagation.

Fault throws for the model with two cross-cutting faults (Fig. 1b; same fault length combination, i.e. 6 and 30 km) display a pattern (Fig. 5b) overall similar to that described above in Fig. 5a. At 1.5% bulk extension, the large fault also shows much greater throw than the small fault. However, the magnitudes of the throws differ from those of the model above (Fig. 5a). The maximum and minimum throws of the large fault in the current model are 166 m and 85 m, respectively, greater than those from the parallel-fault model. For the small fault, the maximum and minimum throws are 31 m and 20 m, respectively, also indicating a greater total-throw (integrated along length) than in the parallel-fault model (see Fig. 5a and b).

To further explore the effects of fault length on fault throw, we have constructed a pair of corresponding models (i.e. two parallel fault and two cross-cutting fault cases with the same fault spacing)

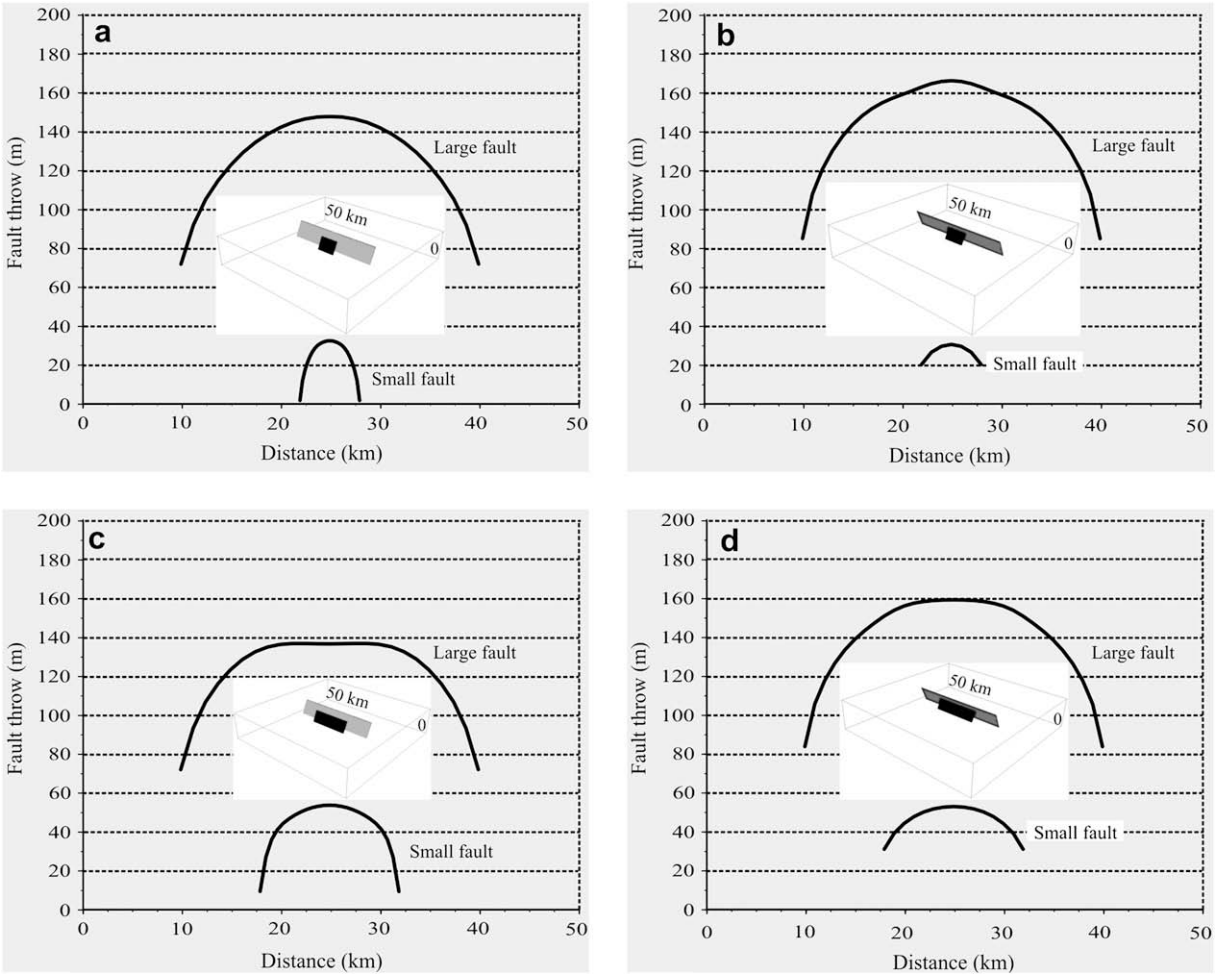

Fig. 5. Distributions of throws along faults (the top sandstone level) for four models at 1.5% bulk extension. (a) Two parallel faults (6 and 30 km long, spacing = 2.5 km). (b) Two cross-cutting faults (6 and 30 km long). (c) Two parallel faults (14 and 30 km long, spacing = 2.5 km). (d) Two cross-cutting faults (14 and 30 km long). The insets illustrate initial fault geometries. Fault throw here is the vertical component of fault displacement.

with a fault strike length combination of 14 and 30 km (Fig. 5c and d). It is noted that at 1.5% bulk extension, a reduction in fault length contrast between the large and small faults leads to a decrease in throw contrast between the two faults. In both the parallel-fault case (Fig. 5c) and cross-cutting fault case (Fig. 5d), the maximum throws along the large fault decreased slightly, whereas throws along the small faults increased, in comparison with the models with the length combination of 6 and 30 km (see Fig. 5a and b). We also note that the throws of both large and small faults in the cross-cutting fault model (Fig. 5d) are greater than those in the corresponding parallel-fault model (Fig. 5c), consistent with the results described above.

4.2. Effects of fault spacing

Spacing is another factor that could affect strain partitioning between fault members. To explore this effect, four models containing a pair of parallel large (30 km long) and small (6 km long) faults at a spacing of 1.0, 2.5, 5.0 and 10.0 km, respectively, have been analysed. Fig. 6 gives the fault throw distribution patterns from these models at 1.5% bulk extension.

At a spacing of 1.0 km, the small fault shows a maximum throw of 15 m at its centre location and almost zero throw at its tips (Fig. 6a). In contrast, the large fault shows much greater throw with a maximum throw of 145 m and minimum throw of 72 m at its original tips. The throw distribution along the large fault displays a bi-modal pattern, with the throw maxima located at the flanks of the fault central location. The trough in the throw distribution profile for the large fault coincides with the length span of the small fault. This suggests two-fold interactions in the case where a small fault exists in close distance to a large fault: 1) the small fault is well protected by the large fault and displays very small throw; and 2) the presence of the small fault can also cause local throw drop along the large fault. Increasing spacing to 10 km through 2.5 and 5.0 km generally leads to the increase of throws on the both faults (Fig. 6b–d). Analyses indicate that for the large fault, the maximum throw is 147, 148 and 154 m at spacings of 2.5, 5 and 10 km, respectively, which are all greater than the maximum throw in the case of a spacing of 1.0 km. Fault throws for the small fault in the larger spacing models are also greater than in the spacing of 1.0 km model.

4.3. Effects of fault strike overlap geometry

In all the models presented above, the small fault has a full strike-overlap relationship with the large fault. We now explore a group of models with faults partially overlapped or not overlapped at all along their strike direction. The first model (Fig. 7a) simulates a case where two parallel faults of the same length (14 km) are partially overlapped by 6 km (spacing = 2.5 km). Fault

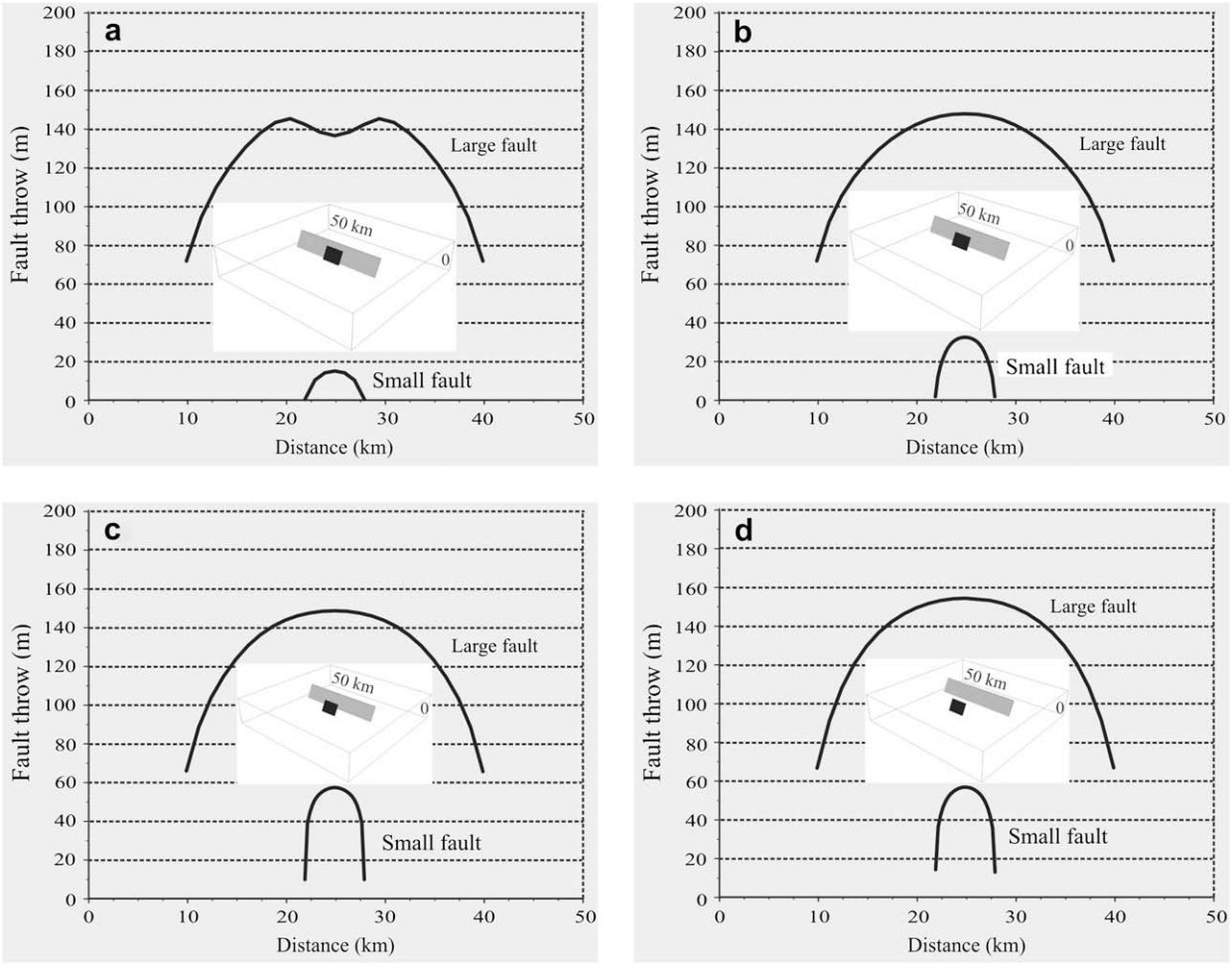

Fig. 6. Distributions of throws along faults (the top sandstone level) in four models with two parallel faults and the same fault length combination (6 and 30 km) but different fault spacing. Fault spacings are1.0, 2.5, 5.0 and 10 km in (a), (b), (c) and (d), respectively. The insets illustrate initial fault geometries. The results are for the 1.5% bulk extension stage.

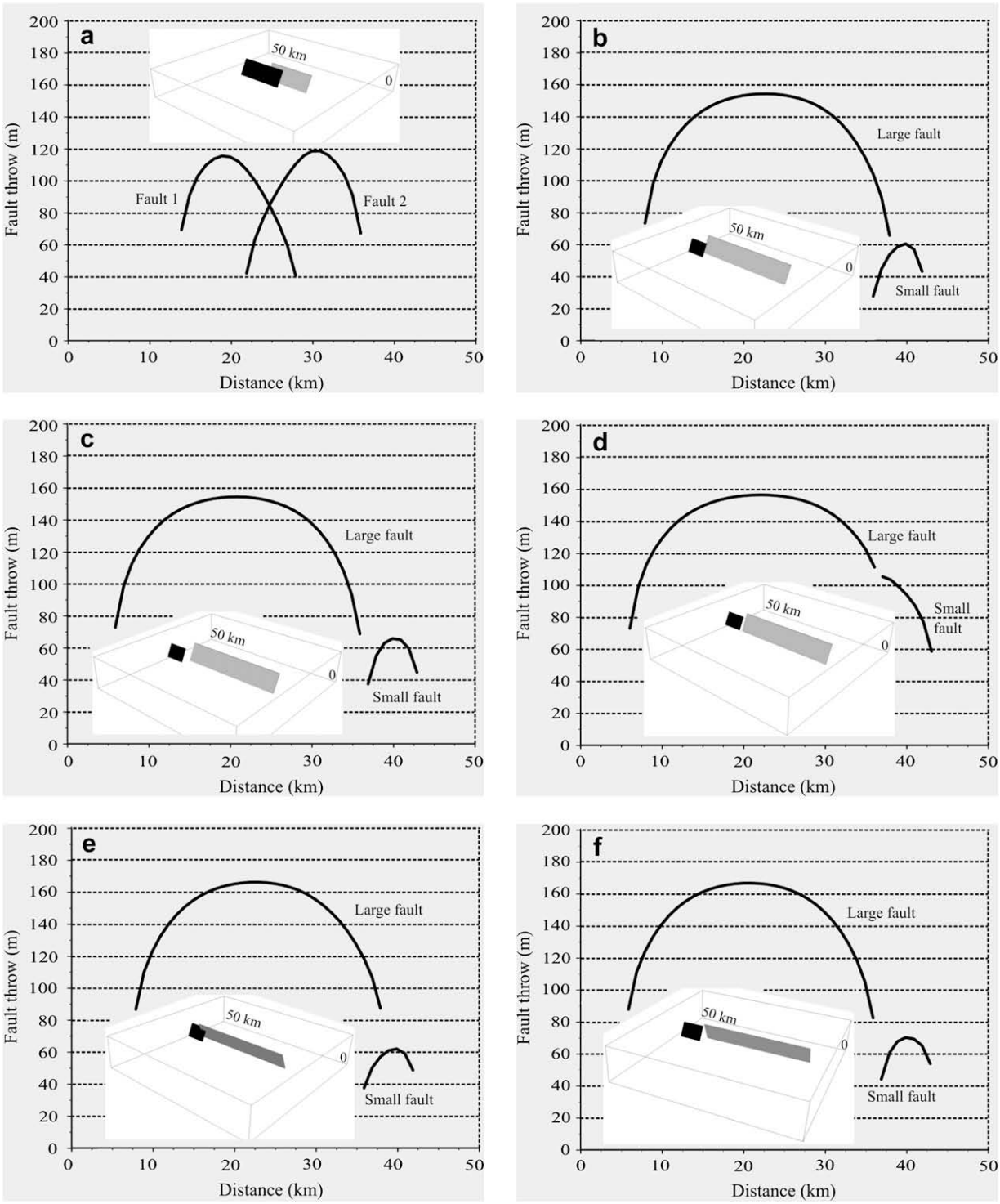

Fig. 7. Distributions of throws along faults in six models with a variety of fault alignment patterns. (a) Two parallel faults of 14 km long, partially overlapped by 6 km. (b) Two parallel faults of 6 and 30 km long, partially overlapped by 2 km. (c) Two parallel faults of 6 and 30 km long with no overlap (separation is 1 km at adjacent fault tips). (d) Two parallel faults of 6 and 30 km long, striking along the same strike line (separation is 1 km at adjacent fault tips). (e) Two cross-cutting faults of 6 and 30 km long, partially overlapped by 2 km. (f) Two cross-cutting faults of 6 and 30 km long with no overlap (separation is 1 km at adjacent fault tips). Fault spacing is 2.5 km in (a)–(c). The insets illustrate initial fault geometries. The results are for the 1.5% bulk extension stage.

throw distributions at 1.5% bulk extension display a roughly mirror-image pattern between the two faults. The throw maxima of the both faults are shifted away from fault central locations towards their non-overlapping ends. In addition, the throws at their overlapping ends are much smaller than at their non-overlapping ends, apparently due to fault interaction and strain sharing there.

The next model (Fig. 7b) simulates a scenario with two parallel faults of different lengths (6 and 30 km, respectively; spacing = 2.5 km), which are partially overlapped by 2 km. As is obvious in Fig. 7b, the change of fault lengths and incorporation of a large length contrast led to large partitioning of throw values between the two faults. At 1.5% bulk extension, the throws along

the large fault are much greater than those along the small faults, again confirming the importance of fault length in strain accommodation. Throw distribution along the both faults are also asymmetric, with the occurrence of lower throws at their overlapping ends as compared to the non-overlapping ends. This is consistent with the results of the model above (Fig. 7a). In a model variation (Fig. 7c), we shifted the small fault in its strike direction so that it does not overlap with the large fault (now with a strike separation of 1.0 km). The patterns of fault throw (Fig. 7c) for the two faults at 1.5% extension are similar to that of the previous model (Fig. 7b). The only difference is that throws along the smaller fault are increased marginally due to less fault interaction in this non-overlap case. In yet another model variety (Fig. 7d), the smaller fault was shifted in the dip direction so that it aligns in the same strike line as the large fault (i.e. spacing = 0, strike separation = 1.0 km). The throw distribution patterns (Fig. 7d) are very different to that of the previous model (Fig. 7c). Now the throws at their adjacent tips are much greater than at the other tips. The two faults appear to behave as one single longer fault, reflected by one broad arched throw profile with only a minor discontinuity at their adjacent tips.

Two models with cross-cutting faults (Fig. 7e and f) were also performed, which have the same fault length combination (6 and 30 km) and overlap conditions (2 km overlap and non-overlap) as two of the parallel-fault models above (Fig. 7b and c). The throw results of the models at 1.5% bulk extension show that smaller throws occurred along the small fault in the partial-overlap case (Fig. 7e) than in the non-overlap case (Fig. 7f), consistent with the results of their corresponding parallel-fault models above. It is again noted that the fault throws in the cross-cutting fault models are generally greater than in the corresponding parallel-fault models (e.g. compare Fig. 7f and c).

4.4. Stress patterns

Shear stresses are analysed for two models with a pair of parallel and cross-cutting faults (large at 30 km and small at 6 km in length), respectively. Fig. 8 illustrates section views (Fig. 8a and c) and plan-views (b and d) of shear stress patterns for the models. In each model, both large and small faults at the 1.5% bulk extension stage (post-failure) are generally dominated by lower shear stress, in comparison with host rocks at similar depth levels. Small faults seem to have marginally lower shear stress than the large faults (e.g. at the shale level or below) as more clearly shown in the section plots (Fig. 8a and c). Higher shear stresses are observed in the hanging-wall block near the lower tips of faults in the sandstone horizons, in clear contrast to lower shear stresses at locations of adjacent footwall blocks. However, shear stress patterns at shallower levels in the carbonate unit are somewhat different, where the footwall sides of the faults in both models seem to show marginally higher stresses (Fig. 8a and c). In particular, a major stress low is observed in the top hanging-wall area of the large fault adjacent to the elevated footwall block (see the parallel-fault model in Fig. 8a). These features are most likely determined by the kinematics of fault block rotation associated with normal faulting. On the plan-view horizons, the major feature illustrated by plots of shear stresses at a level in the carbonate unit (Fig. 8b and d) is high shear stress localisation near the tips of large faults (localisation at the tips of small faults is minor).

To understand the evolution of shear stress in fault zones with time, the variation of shear stresses versus bulk extension in large and small faults (for locations in the shale levels) is plotted in Fig. 9. In both the parallel-fault models and cross-cutting fault models, shear stresses in large faults increased faster and attained the failure stress earlier (at about 0.1% bulk extension), than in small faults (at >0.2% bulk extension). Post-failure shear stress development in both large and small faults is characterized by a rapid stress drop, followed by slower further stress drop or relatively stable stress patterning. Some minor stress rise is observed along the large fault of the parallel-fault model (Fig. 9a) after large post-failure stress drop. This coincides with the increase of strain rate along the large fault after 1% bulk extension (see Fig. 4). Therefore, we speculate this stress increase on the large fault is due to the need of strain rate increase along the large fault. It is also noted that shear stress drop in the small faults is greater than that in the large faults and as such, the small faults have smaller shear stresses. This seems to reflect the fact that the smaller fault has smaller and decreasing

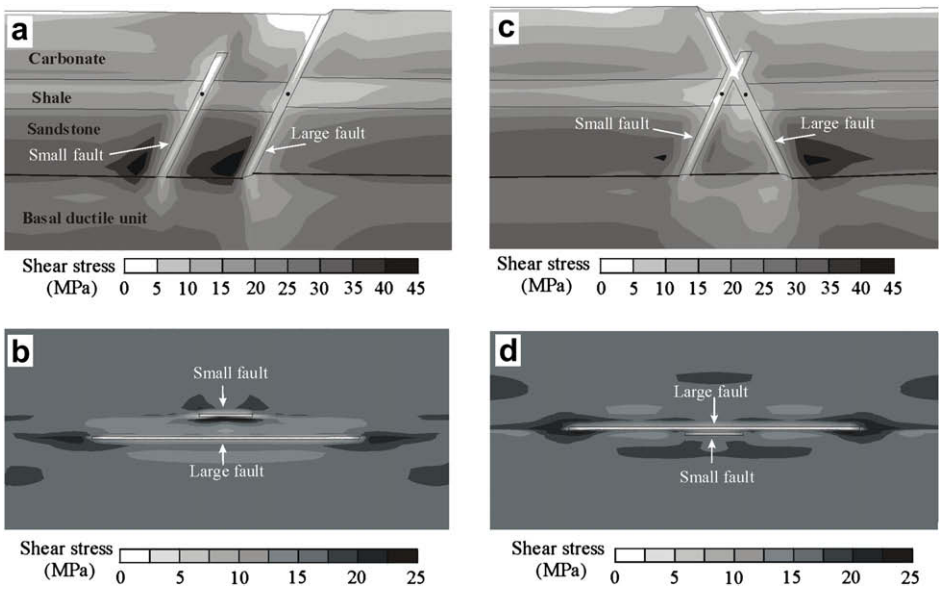

Fig. 8. Section views (a) and (c) and plan-views (b) and (d) of shear stress contours for two models at 1.5% bulk extension. (a) and (b) A model with two parallel faults. (c) and (d) A model with two cross-cutting faults. The section views are along the A–B section of Fig. 1; horizontal lines show the boundaries of the shale unit. The plan-views are for a horizon in the carbonate unit (at a ~1350 m depth level below the top surface of the footwall block of the large fault). The dots on (a) and (c) show the locations for stress tracking.

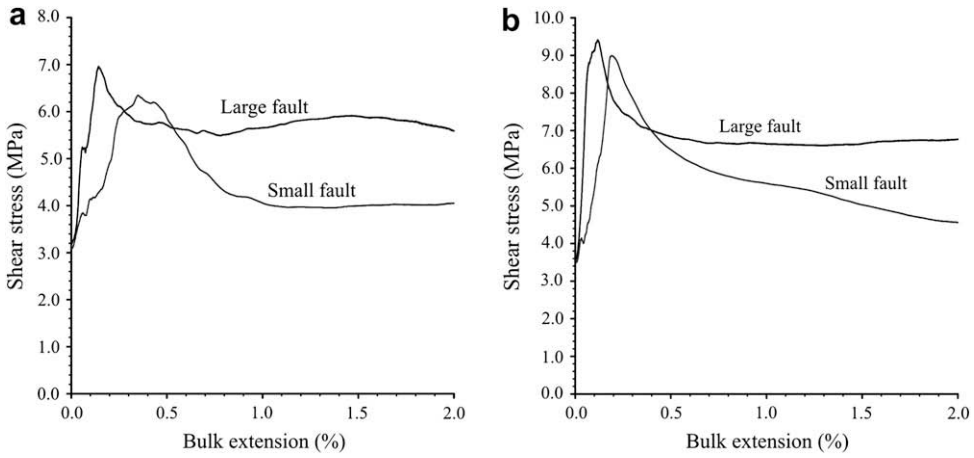

Fig. 9. Curves of shear stress versus bulk extension for the models with two parallel faults (a) and two cross-cutting faults (b), respectively. Stress tracking is for a fault central location at the shale layer level (see dots in fault zones in Fig. 8a and c).

strain rate during the model extensional history, in comparison with the large fault, and is hence less energy demanding.

4.5. Fluid flow patterns

The model results above demonstrate that fault length is the most important factor controlling the partitioning of bulk extensional strain and localisation of shear strain. As described in the methodology section, permeability enhancement in faults in these models was made to be proportional to shear strain. As such, the patterns of fluid flow in the models are also strongly influenced by the interaction of faults of varying lengths. Fig. 10 presents the section views of fluid flow patterns (fluid flow velocity contours and vectors) for the parallel-fault model and cross-cutting fault model (see Fig. 1 for initial geometries and Fig. 3 for deformation patterns), in which an initially slightly over-pressured fluid pore pressure system was incorporated (see Fig. 2). It is noted that in both the parallel fault and cross-cutting fault cases, upward fluid migration from the sandstone or reservoir horizon predominates along the large fault. In contrast, fluids tend to migrate across the small fault at the reservoir level without major upward flow. There appears to be favourable upward fluid flow from the footwall side of the large fault at the sandstone (reservoir) horizons, where normal displacement resulted in relatively elevated sandstone horizons and larger opening into the fault zone from the sandstone unit. Such areas may accumulate more fluids, at least for some period of extensional reactivation. It should be emphasized that the greater permeability increase in the portion of the large fault within the shale horizon (initially low permeability) is the control for the upward flow of fluids in the sandstone unit and this is related to high shear strain localisation there.

At the shallow levels in the carbonate unit, topography generated by fault movement exerts significant control on fluid flow patterns (Fig. 10). There is strong, predominantly down-ward fluid flow towards the fault zones of the larger faults (most dilatant, see Fig. 3) and footwall side, adjacent to the elevated hanging-wall block. In the footwall side, these fluids mix with the fluids discharged along the large fault and also the fluids laterally from the far-field areas of the basin. Such fluid circulation patterns clearly reflect the topographic drive. It should be pointed out that the fluid flow patterns described above possibly only apply to the settings of active extensional reactivation where fault deformation generates large shear and dilatancy, and enhances permeability. Such fluid flow fields will likely dissipate with time once extension ceases.

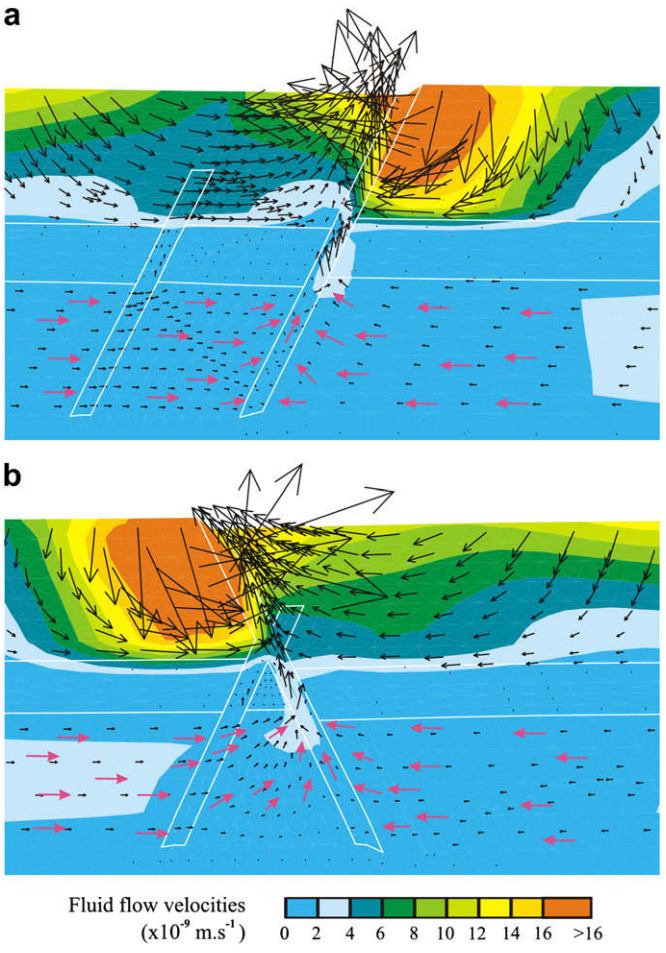

Fig. 10. Section plots of fluid flow velocity magnitudes (color shaded contours) and flow vectors (black arrows) for the models with two parallel faults (a) and two cross-cutting faults (b) at 1.5% bulk extension. Fig. 1 shows the initial geometries of the model and the A–B line gives the location of the plotted section. Note the pink arrow only illustrate the patterns of fluid flow direction in the sandstone (velocity arrows in back are hard to see due to scaling). A few very high velocity arrows near the top ends of the large faults are excluded due to scaling, but flow velocity magnitudes are given by contour plots.

5. Discussion

5.1. Strain localisation on faults

The present numerical models demonstrate that the pre-existing (i.e. prior to a reactivation event) length of faults in a fault population is the primary control for the strain distribution during extensional reactivation. In all cases simulated, strain was preferentially and progressively localised on the longer fault in the models. With greater length contrast between adjacent faults (either parallel or cross-cutting), the more strain will be partitioned towards the longer fault. This behaviour is interpreted to occur because movement on the longer faults is a more efficient means of relieving stress built up in the rock mass. A greater amount of stress is relieved within the rock volume by slip on a longer fault for doing the same amount of work in overcoming the frictional strength of the faults and deforming fresh rock during propagation of the fault tips. The other major resistance to fault movement, in addition to fault plane friction, is the "pinning" from the tips of a fault. For a shorter fault, the central portion of the fault is closer to the tips and is likely subjected to more resistance to movement. In contrast, the central portion of a longer fault is more remote from its tips and therefore has more freedom to move and deform. The movement and deformation of rocks in the fault central portion could feed back into the mechanical status at fault tips and then possibly affect fault propagation. Other factors, such as the location of faults relative to other faults in the population (e.g. overlapping or along-strike) and geometry (e.g. parallel or cross-cutting) also have significant impact on the distribution of strain. The strain localisation results are consistent with previous numerical modelling work (e.g. Cowie, 1998; Walsh et al., 2001); however, the fault geometries and deformation style modelled for this study are more representative of reactivated rift systems. Furthermore, the strain and stress relationships are more clearly demonstrated here.

Stewart (2001) showed that the ideal distribution of displacement along a single extensional fault is characterized by the maximum displacement at the middle of the fault and zero displacement at the tips. This results in a smooth arched displacement profile. The fault throw profiles displayed by the current models both with parallel and cross-cutting fault faults are consistent with this pattern (Fig. 5). Our models also show that the throw profiles in the cases with larger fault length contrast (see Fig. 5a and b) display a sharper arc shape, whereas the profiles for the cases with smaller fault length contrast show a wider plateau shape (Fig. 5c), particularly for the large fault. This seems to be controlled by the relative length of the small fault, essentially reflecting the interaction and strain sharing between adjacent large and small faults. In addition, our models show that interaction between adjacent faults increases with the decrease of fault spacing. When the large and small faults are very close (Fig. 6a), not only do the small fault shows very small throw, but also the large fault has smaller maximum throw and a bi-modal throw profile. The small fault is well protected in this case. Increasing the spacing seems to increase the freedom of both faults to move and leads to greater fault throws (Fig. 6b–d).

The behaviours of strain sharing between adjacent faults in a fault population are further illustrated by the results of the models with partial fault overlap or with no overlap but small separation (Fig. 7). This is dominantly reflected by the decreased throw distribution at the overlapped ends or adjacent ends of such faults. This effect is particularly profound on smaller faults. However, the situation becomes different when two parallel faults extend along the same strike line but with small separation at their adjacent ends (i.e. zero spacing; Fig. 7d). In this case, fault throws are greater at the adjacent ends than at the other ends, namely, the two faults behave almost as one single fault. The current results also show that cross-cutting faults generally display somewhat greater throw than the corresponding parallel fault case, given the same length contrast. This seems to suggest that the cross-cutting fault case is relatively more favourable for fault movement than the parallel fault case. However, this implication needs to be explored by more future work with consideration of wider range of fault strike length and depth variations.

Walsh et al. (2002) suggested normal faults maintain near-constant fault lengths during growth with the growth essentially accommodated by displacement (increase in displacement/length ratio). Our model results here suggest that this hypothesis might be true for small faults which are protected by large faults and display small throw (in particular near their original ends, see Fig. 5a), but very unlikely for large faults experiencing extensional reactivation. The large faults modelled here display quite large throw near their original ends (Fig. 5) and high shear stresses exist near these ends (Fig. 8b and d). These observations suggest that the large fault would have grown in strike length during extensional reactivation.

5.2. Comparison with natural systems

Localisation of strain on to larger faults is consistent with observations from natural fault sets. In the Timor Sea, for example, Meyer et al. (2002) and Gartrell et al. (2005) showed that longer rift-phase (Jurassic) faults tend to display relatively high displacement rates, greater accumulated displacements and prolonged sedimentary growth histories during post-rift (Neogene) reactivation than shorter rift faults in the population. The longer sedimentary growth histories exhibited by the larger faults represents continued fault displacement at the seafloor. In contrast, the upper tips of the smaller rift faults typically terminate a significant distance below the seafloor, indicating either that these faults have become dormant, or that sedimentation has out paced fault displacement.

The observed heterogeneous strain distribution has a significant impact on hydrocarbon prospectivity in the Timor Sea, as well as other basins where post-charge fault reactivation has occurred (Gartrell et al., 2005, 2006). Comparisons between fault histories and the distribution of current and palaeo-oil accumulations in the Timor Sea indicate that the total amount of displacement on a trap bounding fault during reactivation is critical for hydrocarbon preservation potential (Gartrell et al., 2005, 2006). From a trap integrity perspective, the numerical modelling presented here demonstrates that higher potential for hydrocarbon preservation will occur where large faults overlap smaller faults. This is consistent with the structural models of hydrocarbon preservation for the Timor Sea (Fig. 11; Gartrell et al., 2005, 2006). However, the numerical modelling performed demonstrates that a number of factors (e.g. fault length, location, spacing and geometry) interact, sometimes in a complex way, to control the strain distribution. Hence, the numerical approach may help to better quantify strain distributions and associated fault leakage potential in relatively complex fault populations.

Gartrell et al. (2006) proposed that faults with greater displacements accumulated during reactivation stood a higher chance of developing a connected fault fracture network across top seal units, thus creating potential fluid conduits. This behaviour is incorporated in the modelling performed for this study by implementing a somewhat arbitrary relationship between permeability and shear strain. As a result, higher fluid flow rates were associated with the larger faults. In addition to higher shear strain, the larger faults also exhibit greater dilation and larger stress drops, which also contributes to higher fluid flow. It is also possible that at shear strains above a certain threshold that fault permeabilities may start

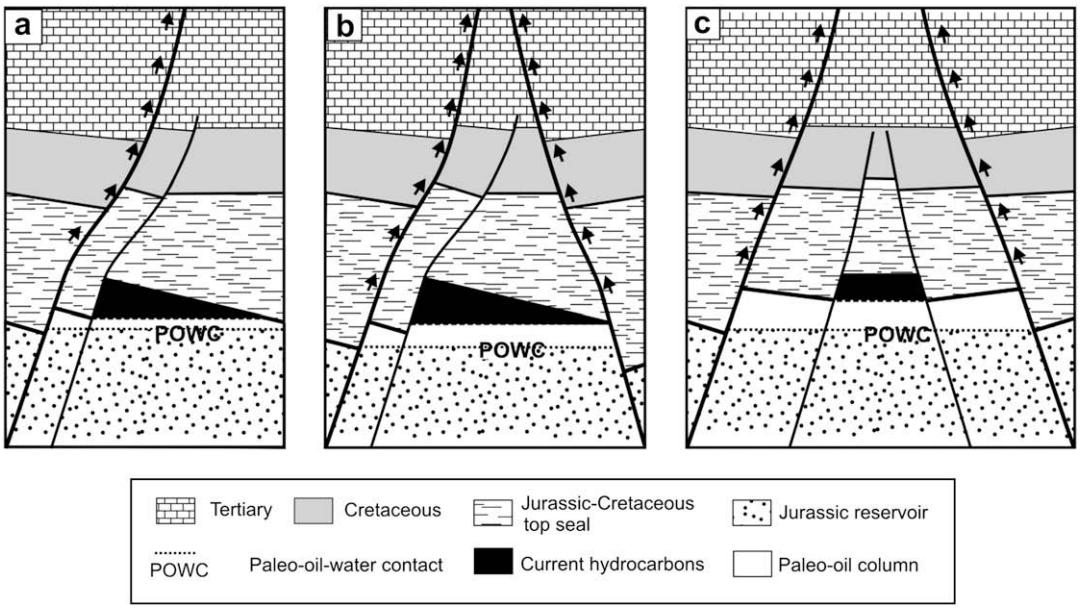

Fig. 11. Several structural models about fault control on hydrocarbon leakage and preservation in the Timor Sea (see Gartrell et al., 2005, 2006 for details). (a) Shielded fault block (Skua area); (b) partially shielded horst (Laminaria High area); and (c) shielded sub-horst (Buffalo area). Arrows illustrate hydrocarbon leakage path (along larger faults) and black areas show the currently preserved hydrocarbon columns (bound by small faults).

to reduce (e.g. Holland et al., 2006). Further work is required to establish more realistic relationships between fault permeability and controlling factors such strain, stress, rock composition (e.g. clay content) which can be incorporated into numerical models of this type.

The larger faults will also tend to propagate higher into the overburden and towards the surface during reactivation. Such characteristics will tend to further enhance the ability of these faults to leak hydrocarbons out of traps due to better access to discharge sites (e.g. shallower reservoirs or the water column). In contrast, shorter faults with lower reactivational displacements do not tend to propagate as high into the overburden and will stand a greater chance of being buried by syn-kinematic sedimentation. As a result, less efficient discharge of hydrocarbons is likely via these less heavily reactivated faults. As described above, sharing of bulk strain between adjacent faults results in reduced displacements on individual faults in a fault population, particularly along overlapped segments. This may in turn reduce the leakage potential of these faults. Therefore, greater opportunity for hydrocarbon preservation during fault reactivation will occur where fault-bound traps are located in regions with several overlapping faults. The Laminaria High area in the Timor Sea is a good example of such a region where relatively high drilling success rates are encountered in association with several overlapping and interacting reactivated faults (Gartrell et al., 2005, 2006).

In general, the numerical experiments support the structural and hydrocarbon preservation model proposed by Gartrell et al. (2006), by demonstrating the longer faults localise much of strain/displacement and act as main upward fluid flow conduits (Fig. 11).

Having considered that longer faults represent greater risk to trap integrity and hydrocarbon preservation, it is also important to realize that in some situations these "leaky" faults could provide migration pathways for transporting hydrocarbons from deep reservoirs to shallower traps. For example, Fu et al. (2006) reported that the Hutubi oil and gas reservoir in northwest China was formed as a result of the upward migration of oil and gas from the Jurassic–Cretaceous formations (traps) along regional major faults into the Tertiary trap structures during the Himalayan tectonic event. Furthermore, some degree of hydrocarbon leakage may be a favourable condition where gas is leaked preferentially to oil, reducing the effects of gas flushing and allowing oil columns to be preserved.

6. Conclusions

The current model results demonstrate that the initial length of faults in the modelled fault population is the primary control in determining the distribution of strain between faults and in transporting fluids through the seal from the reservoir horizon. During extensional reactivation, longer faults tend to accommodate greater shear strain and generate greater displacements than smaller faults in the models. The greater the length contrast between adjacent faults, the greater the degree of strain partitioning. This behaviour applies to both the parallel and cross-cutting fault geometries, and can be attributed to the fundamental mechanism of strain sharing (i.e. sharing of bulk extension) among the members of a fault population. Fault displacements along faults in the cross-cutting fault model are generally greater than those in the corresponding parallel-fault models.

The models also show that spacing between adjacent faults is another factor that affects strain partitioning between fault members. For a given fault length contrast, interaction between adjacent faults decreases with the increase of the fault spacing. In the case where a small fault is located close to a large fault (i.e. small spacing), the small fault displays very small displacement due to the protection of the large fault. Moreover, the large fault also displays anomalous reduction of fault throw over its segment overlapped with the small fault and its throw profile exhibits a bi-modal pattern (i.e. two maxima), reflecting the effect of interaction with the small fault. A series of models show that increasing the spacing in this scenario increases the freedom of both faults to move and leads to greater fault throw in both the large and small faults.

Fault strike overlap geometry also influence strain distribution along faults. This effect is mainly expressed as the reduction of fault throw in the overlapped fault segment. In the cases where two

faults are partially overlapped, fault throws at the overlapped fault ends are clearly smaller than the other ends and the maximum throw on each fault is shifted away from the fault central location towards the non-overlap ends. This case can be extended to non-overlap but adjacent faults, with the adjacent fault ends showing smaller throw. Strain sharing is also the cause for such features.

The length of faults also controls fluid flow patterns during extensional reactivation in the models. Large faults are the main conduit for fluid transport, and this is expressed as strong upward fluid migration from the sandstone unit (reservoir horizon) along the reactivated large fault through the shale. These upward-migrated fluids mix with normal faulting related, topographic-driven flow in the carbonate unit at shallow levels. Current modelling results on fluid flow are consistent with and support a hydrocarbon preservation model for the Timor Sea (Gartrell et al., 2005, 2006), derived from structural analyses and seismic interpretation. That is, the strain localisation and displacement on a trap bounding fault during reactivation are important for hydrocarbon preservation potential and hydrocarbons tend to be preserved in the traps bound by smaller faults with low post-rift displacements, commonly overlapped by larger high displacement faults.

Acknowledgements

We would like to thank Woodside, Schlumberger, Origin, Santos, Chevron, Primary Industries and Resources of South Australia (PIRSA), and Anadarko Petroleum Corporation for financial support of the Integrated Predictive Evaluation of Traps and Seals (IPETS) Consortium. IPETS is also supported financially by the CSIRO Wealth from Oceans Flagship research program and the Western Australian Energy Research Alliance (WA-ERA). Woodside Energy Limited and BHP-Billiton are duly thanked for providing the seismic data shown in Fig. 1c and d respectively. Stefan Schmalholz and Jianwen Yang are thanked for their constructive reviews of the manuscript.

References

Buchmann, T.J., Connolly, P.T., 2007. Contemporary kinematics of the Upper Rhine Graben: a 3D finite element approach. Global and Planetary Change 58, 287–309.

Buchmann, T.J., Peters, G., Connolly, P.T., 2008. Recent faulting in the Upper Rhine Graben (Germany): a 3D finite element approach to predict fault reactivation. Proceedings of 42nd US Rock Mechanics Symposium and 2nd US–Canada Rock Mechanics Symposium (June 29–July 2, 2008), paper no.: ARMA08-244, 5 pp.

Connolly, P., Cosgrove, J., 1999a. Prediction of static and dynamic fluid pathways within and around dilational jogs. In: McCaffrey, K.J.W., Lonergan, L., Wilkinson, J.J. (Eds.), Fractures, Fluid Flow and Mineralization. Geological Society, London, Special Publications, vol. 155, pp. 105–121.

Connolly, P., Cosgrove, J., 1999b. Prediction of fracture-induced permeability and fluid flow in the crust using experimental stress data. AAPG Bulletin 83, 757–777.

Cowie, P.A., 1998. A healing-reloading feedback control on the growth rate of seismogenic faults. Journal of Structural Geology 20, 1075–1087.

Cox, S.F., 1995. Faulting processes at high fluid pressures: an example of fault valve behavior from the Wattle Gully Fault, Victoria, Australia. Journal of Geophysical Research 100, 12841–12859.

Cundall, P.A., Board, M., 1988, A microcomputer program for modelling large-strain plasticity problems. In: Swoboda, G. (Eds.), Proceedings of the Sixth International Conference on Numerical methods in Geomechanics: Numerical Methods in Geomechanics. vol. 6, pp. 2101–2108.

Fu, X.W., Chen, S.J., Wang, X.L., Zeng, J., 2006. Geology of the Hububi gas reservoir in the southern margin of the Junggar basin, Northwest China. 2006 AAPG Interantional Conference and Exhibition abstract volume/CD, 5–8 November 2006, Perth, Australia, 7 pp.

Gartrell, A., Bailey, W.R., Brincat, M., 2005. Strain localization and trap geometry as key controls on hydrocarbon preservation in the Laminaria high area. APPEA Journal (Australian Petroleum Production and Exploration Association) 45, 477–492.

Gartrell, A., Bailey, W.R., Brincat, M., 2006. A new model for assessing trap integrity and oil preservation risks associated with post-rift fault reactivation in the Timor Sea. AAPG Bulletin 90, 1921–1944.

Gartrell, A., Zhang, Y., Lisk, M., Dewhurst, D.N., 2004. Fault intersections as critical hydrocarbon leakage zones: integrated field study and numerical modeling of an example from the Timor Sea, Australia. Marine and Petroleum Geology 21, 1165–1179.

Garven, G., Bull, S.W., Large, R.R., 2001. Hydrothermal fluid flow models of stratiform ore genesis in the McArthur Basin, Northern Territory, Australia. Geofluids 1, 289–311.

Hobbs, B.E., Mühlhaus, H.-B., Ord, A., 1990. Instability, softening and localisation of deformation. In: Knipe, R.J., Rutter, E.H. (Eds.), Deformation Mechanisms, Rheology and Tectonics. Geological Society, London, Special Publication, vol. 54, pp. 143–165.

Holland, M., Urai, J.L., van der Zee, W., Stanjek, H., Konstanty, J., 2006. Fault gouge evolution in highly overconsolidated claystones. Journal of Structural Geology 28, 323–332.

Itasca, 2005. FLAC3D: Fast Lagrangian Analysis of Continua in 3 Dimensions, User Manual, Version 3.1. Itasca Consulting Group, Inc., Minneapolis.

Jaeger, J.C., Cook, N.G.W., 1979. Fundamentals of Rock Mechanics, third ed. Chapman and Hall, London.

Mandl, G., 1988. Mechanics of Tectonic Faulting. Elsevier, Amsterdam.

McClay, K., Bonora, M., 2001. Analog models of restraining stepovers in strike-slip fault systems. AAPG Bulletin 85, 233–260.

McLellan, J.G., Oliver, N.H.S., Schaubs, P.M., 2004. Fluid flow in extensional environments; numerical modeling with an application to Hamersley iron ores. Journal of Structural Geology 26, 1157–1171.

Meyer, V., Nicol, A., Childs, C., Walsh, J.J., Watterson, J., 2002. Progressive localisation of strain during the evolution of a normal fault population. Journal of Structural Geology 24, 1215–1231.

O'Brien, G.W., Lisk, M., Duddy, I.R., Hamilton, J., Cowley, R., 1999. Plate convergence, foreland development and fault reactivation: primary controls on brine migration, thermal histories and trap breach in the Timor Sea. Marine and Petroleum Geology 16, 533–560.

Ord, A., 1991. Deformation of rock: a pressure-sensitive, dilatant material. Pure and Applied Geophysics 137, 337–366.

Otto, C., Underschultz, J., Hennig, A., Roy, V., 2001. Hydrodynamic analysis of flow systems and fault seal integrity in the Northwest Shelf of Australia. Australian Petroleum Production and Exploration Association Journal 41 (1), 347–365.

Schaubs, P.M., Rawling, T.J., Dugdale, L.J., Wilson, C.J.L., 2006. Factors controlling the location of gold mineralisation around basalt domes in the Stawell corridor: insight from coupled 3-D deformation–fluid-flow numerical models. Australian Journal of Earth Sciences 53, 841–862.

Sibson, R.H., 1985. A note on fault reactivation. Journal of Structural Geology 7, 751–754.

Sorjonen-Ward, P., Zhang, Y., Zhao, C., 2002. Numerical modeling of orogenic processes and gold mineralization in the southeastern part of the Yilgarn craton, Western Australia. Australian Journal of Earth Sciences 49, 1011–1039.

Stewart, S.A., 2001. Displacement distributions on extensional faults: implications for fault stretch, linkage, and seal. AAPG Bulletin 85, 587–599.

Strayer, L.M., Hudleston, P.J., Lorig, L.J., 2001. A numerical model of deformation and fluid-flow in an evolving thrust wedge. Tectonophysics 335, 121–145.

Underschultz, J.R., Ellis, G.K., Hennig, A., Bekele, E., Otto, C., 2002. Estimating formation water salinity from wireline pressure data: Case study in the Vulcan Sub-basin. In: Keep, M., Moss, S.J., (Eds.), The Sedimentary Basins of Western Australia 3: Proceedings of The Petroleum Exploration Society of Australia Symposium, Perth, West Australia, 2002, pp. 285–303.

Vermeer, P.A., de Borst, R., 1984. Non-associated plasticity for soils, concrete and rock. Heron 29, 1–64.

Walsh, J.J., Childs, C., Meyer, V., Manzocchi, T., Imber, J., Nicol, A., Tuckwell, G., Bailey, W.R., Bonson, C.G., Watterson, J., Nell, P.A., Strand, J., 2001. Geometric controls on the evolution of normal fault systems. In: Holdsworth, R.E., Strachan, R.A., Magloughlin, J.F., Knipe, R.J. (Eds.), The Nature and Tectonic Segnificance of Fault Zone Weakening. Geological Society, London, Special Publications, vol. 186, pp. 157–170.

Walsh, J.J., Nicol, A., Childs, C., 2002. An alternative model for the growth of faults. Journal of Structural Geology 24, 1669–1675.

Yang, J., Latychev, K., Edwards, R.N., 1998. Numerical computation of hydrothermal fluid circulation in fractured earth structures. Geophysical Journal International 135, 627–649.

Yang, J., Large, R.R., Bull, S.W., 2004. Factors controlling free thermal convection in faults in sedimentary basins: implications for the formation of zinc-lead mineral deposits. Geofluids 4, 237–247.

Zhang, S., Cox, S.F., 2000. Enhancement of fluid permeability during shear deformation of a synthetic mud. Journal of Structural Geology 22, 1385–1393.

Zhang, Y., Mancktelow, Neil S., Hobbs, B.E., Ord, A., Mühlhaus, H.-B., 2000. Numerical modelling of single-layer folding: clarification of an issue regarding the effect of computer codes and the influence of initial irregularities. Journal of Structural Geology 22, 1511–1522.

Zhang, Y., Sorjonen-Ward, P., Ord, A., Southgate, P., 2006. Fluid flow during deformation associated with structural closure of the Isa Superbasin after 1575 Ma in the central and northern Lawn Hill Platform, Northern Australia. Economic Geology101, 1293–1312.

Zhang, Y., Schaubs, P.M., Zhao, C., Ord, A., Hobbs, B.E., Barnicoat, A.C., 2008. Fault-related dilation, permeability enhancement, fluid flow and mineral precipitation patterns: numerical models. In: Wibberley, C.A.J., Kurtz, W., Imber, J., Holdsworth, R.E., Collettini, C. (Eds.), The Internal Structure of Fault Zones: Implications for Mechanical and Fluid-Flow Properties. Geological Society, London, Special Publications, vol. 299, pp. 239–255.